**Noname manuscript No.**
(will be inserted by the editor)

# Numerical Simulations of Turbulent Flame Propagation in a Fan-Stirred Combustion Bomb and Bunsen-Burner at Elevated Pressure

**Feichi Zhang*** · **Thorsten Zirwes** · **Peter Habisreuther** · **Nikolaos Zarzalis** · **Henning Bockhorn** · **Dimosthenis Trimis**

Received: date / Accepted: date

**Abstract** Large eddy simulations (LES) have been carried out to calculate turbulent flame propagation in a fan-stirred combustion bomb and a Bunsen-type burner. Objective of the work is to reveal the main mechanism of increased flame wrinkling due to elevated pressure and to assess the ability of the turbulent flame-speed closure (TFC-class) combustion model to reproduce the enhancement of flame wrinkling or burning rate at elevated pressures. The simulations have been performed for a premixed methane/air mixture at equivalence ratio 0.9 and the pressure has been varied from 1 bar to 5 bar. The turbulent kinetic energy is found to increase with pressure in the high frequency range, indicating reinforced small-scale turbulent fluctuations at elevated pressure. The reason is attributed to the increased turbulent Reynolds number with pressure, which shifts the turbulent energy spectra to the higher wave number range. A reinforced flame wrinkling and an increased total burning rate are obtained at elevated pressure, which is in accordance with results from previous high-pressure combustion experiments. In addition, applying the same method to a quiescent flow in the bomb vessel reveals a decrease of the overall burning rate with pressure, which agrees with the behaviour of laminar flame speed at elevated pressures. Therefore, the beneficial effect of increased burning rate or flame wrinkling at elevated pressure can be explained by the enhanced small-scale turbulent fluctuations along with formation of small-scale vortices and flame structures, which over-compensate the reduced local laminar burning velocity at high pressures. The calculated amplification rates of flame wrinkling factor at increased pressures show a reasonable agreement with measured data for both fan-stirred bomb and Bunsen flame configurations, without using any additional adjusting parameters for considering the pressure effect. The

F. Zhang (corresponding author), P. Habisreuter, N. Zarzalis, H. Bockhorn, D. Trimis
Engler-Bunte-Institute, Division of Combustion Technology, Karlsruhe Institute of Technology, Engler-Bunte-Ring 1, Karlsruhe 76131, Germany
ORCID: 0000-0001-7511-2910
Tel.: +49-721-608-42583
E-mail: feichi.zhang@kit.edu

T. Zirwes
Steinbuch Centre for Computing, Karlsruhe Institute of Technology Karlsruhe Institute of Technology, Hermann-von-Helmholtz-Platz 1, 76344 Eggenstein-Leopoldshafen, Germany

results justify the applicability of the current TFC-LES method for high-pressure combustion processes.

**Keywords** High pressure · Outwardly expanding flame · Turbulent flame-speed closure (TFC) · Large eddy simulation (LES) · OpenFOAM

## 1 Introduction

Most practical combustion processes, such as in internal combustion engines, aircraft engines or gas turbines, take place at highly turbulent flow conditions and elevated pressures, in order to reduce the overall combustor dimension and to achieve higher thermal efficiency. A number of experimental works have been carried out to study the effect of elevated pressure on turbulent flame propagation [1]-[22], which use different burner configurations and fuels. All these previous works have shown an enhanced wrinkling of the flame surface and the formation of smaller scale flame structures at elevated pressure, as illustrated in Fig.1 by an OH-PLIF imaging of a premixed Bunsen-type flame at 1 bar (left) and 10 bar (right) [3].

Among the different explanation attempts, pressure was assumed to promote Darrieus-Landau (DL) instabilities due to the decreased flame thickness [1–5], so that flames at elevated pressure are more prone to hydrodynamic disturbances, leading to the development of flame instabilities with cellular structure. Moreover, it has been found that the Markstein number ($Ma$) decreases or even changes its sign from positive to negative for a broad range of equivalence ratios as the pressure increases, suggesting an increase of local burning speed and a greater tendency toward unstable flame propagation by flow disturbances [6–10]. Additionally, the flame-turbulence interaction and flame wrinkling are reinforced at higher pressures due to decreased Taylor and Kolmogorov length scales, shifting the spectra of turbulent kinetic energy towards higher wave-numbers [11–13]. As the flame thickness is reduced with pressure too, formation of highly convoluted flame front elements

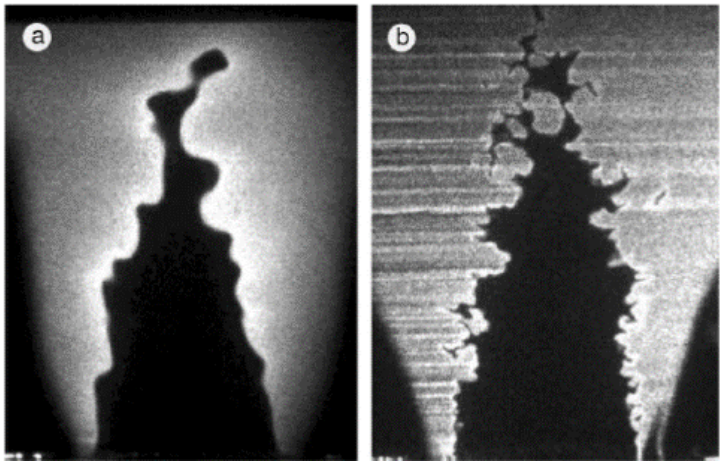


**Fig. 1** OH-PLIF images of turbulent premixed methane/air flames from a Bunsen-type burner at 1 bar (left) and 10 bar (right). This figure is taken from [3].

with large curvature has been detected. Lipatnikov and Chomiak [23] and Creta et al. [24] concluded that the DL instability may not play a substantial role in premixed turbulent combustion. By performing turbulence–flame interaction experiments in DL instability free conditions, Fragner et al. [12] showed that the observed increase in the flame wrinkling and flame surface area with pressure is not due to DL instabilities. Chaudhuri et al. [25] and Yang et al. [26] proposed an extended turbulent regime diagram based on leading-order scaling analysis, which considers the competitive interaction of the DL instability with the intrinsic turbulent flow for the flame corrugation. It has been shown in these works, and further confirmed with experiments for both spherical flame [26] and Bunsen flame [27], that the DL instability is important at weak turbulence conditions with small Karlovitz number $Ka < 1$. Therefore, there is a debate on the basic principles of the effect of pressure on the increase of flame wrinkling.

Although a lot of effort has been put on studying the effect of elevated pressure on the global flame dynamics, experiments in a high-pressure environment are difficult and show a large scattering of measured data. The highly transient flame motion has to be captured with limited optical access as well as limited temporal and spatial resolution. In addition, mostly 2D cuts of the 3D flame surfaces are recorded and used to derive correlations for the turbulent burning velocity as a function of pressure. On the other hand, as the intrinsic flame thickness as well as the smallest length scales of the turbulent flow decrease considerably with pressure, numerical computation of high pressure combustion processes becomes too demanding due to the need for finer grid resolutions. Therefore, it is imperative to develop reliable computational tools for designing future combustor systems operated at high pressure conditions.

For that purpose, large eddy simulations (LES) with a common turbulent flame-speed closure (TFC) combustion model have been conducted for a turbulent outwardly expanding flame in a fan-stirred combustion bomb and a Bunsen-type flame at elevated pressures. The 3D resolution of the turbulent flame enables a more detailed understanding of the behaviour of enhanced flame wrinkling caused by elevated pressure, which complements available experimental data based on detecting 2D planar cuts through the flame surfaces. The TFC-class combustion model is based on one physio-chemical parameter, the turbulent flame speed, for modeling the turbulent mean consumption rate, which is easily accessable from the view point of optical measurement. It has already been extensively used for simulations of turbulent premixed flames [29–36], and is also implemented in the commercial CFD code ANSYS-Fluent. As most of the previous applications have been conducted for atmospheric pressure, the reproducibility of the effect of increased pressure on the flame-turbulence interaction by the proposed TFC-LES approach will be justified in this work. The flame structure has not been compared directly with experiments, as there is no measured data available for the considered bomb setup at high pressures. However, the qualitative behaviour of increased pressure on turbulent flame propagation is compared with existing literature data. In addition, the amplification of total burning rate due to increased pressure is compared quantitatively with measured correlations from literature, yielding reasonably good agreement.

The work is organized as follows: the next two sections introduce the combustion model and numerical setups used for the simulations. Sec.4 presents simula-

tion results for two cases with a fan-stirred combustion bomb and a Bunsen-type burner. The work is then summarized in Sec.5.

## 2 Combustion Modeling

Combustion models are generally applied for numerical simulations of combustion processes, in order to save computational resources required for calculating the reaction rates of each chemical species [37]. One common approach is to reduce the complex reaction system to a global reaction described by a single reaction progress variable $c$, which can be regarded as a normalized reactant or product concentration. It describes the progress of the global reaction from unburnt ($c = 0$) to burnt state ($c = 1$). The species concentrations can be obtained from pre-calculated 1D laminar flames (flamelets), where the species mass fractions are tabulated as functions of $c$ and looked up during the simulation. Following this idea, the combustion model used in this work solves a transport equation for the Favre-filtered progress variable $\tilde{c}$ [35,36]

$$\frac{\partial \bar{\rho}\tilde{c}}{\partial t} + \frac{\partial \bar{\rho}\tilde{u}_i\tilde{c}}{\partial x_i} = \frac{\partial}{\partial x_i}\left((D_L + D_T)\frac{\partial \tilde{c}}{\partial x_i}\right) + \bar{\dot{\omega}}_c \tag{1}$$

$u$ and $\rho$ are the velocity and the density. $D_L$ and $D_T$ are the laminar and turbulent diffusivity. There are different concepts for modeling the turbulent mean rate $\bar{\dot{\omega}}_c$, which considers the effect of flame-turbulence interaction, e.g., the flame surface density or the thickened flame model [37]. In this work, $\bar{\dot{\omega}}_c$ is modeled by

$$\bar{\dot{\omega}}_c = \rho_0 \frac{S_{T,sgs}^2}{D_L + D_T}\tilde{c}(1 - \tilde{c}) \tag{2}$$

with the subgrid scale (sgs) turbulent burning velocity $S_{T,sgs}$ [30,35]

$$\frac{S_{T,sgs}}{S_L} = 1 + \frac{u'_{sgs}}{S_L}\left(1 + Da^{-2}\right)^{-1/4} \tag{3}$$

The combustion model belongs to the turbulent flame-speed closure (TFC-class) model, as Eq.(1) is closed in terms of $S_{T,sgs}$ in the source term $\bar{\dot{\omega}}_c$. In Eq.(2-3), $\rho_0$ is the density of the unburnt mixture, $S_L$ the unstretched laminar flame speed and $u_{sgs}$ the sgs turbulence intensity. The Damköhler number $Da$ is evaluated from the ratio of turbulent and chemical time scales $Da = \tau_T/\tau_C \propto (L_{sgs}/u_{sgs})/(a_0/S_L^2)$, with the thermal diffusivity of the unburnt gas $a_0$. The turbulence parameters $u_{sgs}$ and $L_{sgs}$ are evaluated from the sgs turbulence modeling with $u_{sgs} = \sqrt{k_{sgs}}$ and $L_{sgs} = 0.1\Delta$, where $k_{sgs}$ represents the sgs turbulent kinetic energy and $\Delta$ a characteristic cell length. Assuming a unity turbulent Schmidt number, $D_T$ is modeled by $D_T = \nu_{sgs} = u_{sgs}L_{sgs}$, with the sgs turbulent viscosity $\nu_{sgs}$. In comparison with the general turbulent flame speed considering the overall burning rate, $S_{T,sgs}$ and $\bar{\dot{\omega}}_c$ represent a measure of spatially averaged burning rate within the local cell volume, which are influenced by the grid resolution.

Similar to the eddy break-up (EBU) concept, $\bar{\dot{\omega}}_c$ in Eq.(2) relates the turbulent mean rate to be proportional to the inverse of one characteristic time scale of

the global reaction. In case of strong turbulence intensity with $u_{sgs} \gg S_L$ or $S_{T,sgs} \approx u_{sgs}$, $\bar{\dot{\omega}}_c$ approaches

$$\bar{\dot{\omega}}_c \propto \frac{S_{T,sgs}^2}{D_T} = \frac{u_{sgs} u_{sgs}}{u_{sgs} L_{sgs}} \propto \frac{1}{\tau_T} \tag{4}$$

For weak turbulence conditions with $u_{sgs} \ll S_L$ or $S_{T,sgs} \approx S_L$, $\bar{\dot{\omega}}_c$ asymptotically tends to

$$\bar{\dot{\omega}}_c \propto \frac{S_{T,sgs}^2}{D_L} = \frac{S_L^2}{S_L D_L} \propto \frac{1}{\tau_C} \tag{5}$$

The TFC combustion model along with the procedure of chemistry tabulation proposed in Sec.2 has been implemented into the OpenFOAM framework [38]. The approach has been successfully validated by means of different turbulent premixed flames under atmospheric pressure [33,35,36], where the calculated time mean and root mean square (rms) statistics for the flow velocities and chemical scalars showed a good agreement with measured data. The assessment of its applicability under elevated pressure condition remains task of the present work.

## 3 Simulation Setups

Two flame configurations with a fan-stirred combustion bomb and a Bunsen-type burner are simulated in this work. The computational domain for the bomb case is given by a spherical vessel with a diameter of 160 mm, which is equipped with eight orthogonally oriented fans mounted on the inner wall of the vessel [39]. As illustrated in Fig.2, the axes of the fans are oriented collinear to the diagonals of a cube fitted into the spherical vessel to generate a homogeneous and isotropic turbulent flow field in the core region. The axial distance from one single fan to the opposite one is 133 mm. Each fan has an outer diameter of 45 mm and consists of 6 blades of 19.5 mm length, 6.4 mm depth and 1.8 mm thickness; the surfaces of the non-profiled blades are designed with an angle of attack of 22.5°. The numerical grid consists of 8.6 million tetrahedral elements and is radially refined with the finest grid resolution of $\Delta = 0.2$ mm (cubic root of cell volume) in the core region with $0 < r < 13$ mm (zone I in Fig.2 on the right). The grid size increases with radii to $\Delta = 0.4$ mm for $13 < r < 38$ mm (zone II in Fig.2 on the right) and $\Delta = 0.8$ mm for $38 < d < 80$ mm (zone III in Fig.2 on the right). The regions around the fans have a resolution of $\Delta = 0.8$ mm, too. For the current study, the rotating speed of the fan is set to $\omega = 5000$ revolutions per minute (rpm), yielding a measured root mean square (rms) value of velocity fluctuation at the center of $u' = u_{rms} \approx 1$ m/s [39].

In the second case, the Bunsen burner experimentally studied by Kobayashi et al. [14] has been simulated. As depicted in Fig.3 by the cross-section view of the computational grid, the simulation domain consists of a part of the nozzle with diameter of 20 mm and a free cylindrical domain downstream, with a diameter of 80 mm. Premixed methane/air mixture enters the domain from the inlet, which is located 20 mm upstream of the nozzle exit. The outlet area extends to 160 mm with respect to the nozzle exit. The computational grid consists of approximately 4 million finite volumes, with an equidistant grid resolution of 0.25 mm for the near-nozzle region. The bulk flow velocity at the inlet is set to 2.36 m/s, which

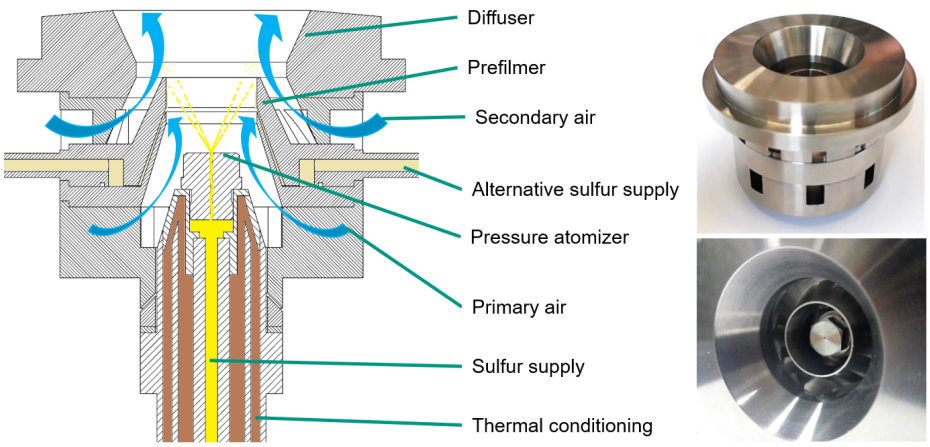


**Fig. 2** Computational domain (left) and grid (right) used for LES of a fan-stirred bomb vessel.

is superimposed with turbulent velocity fluctuations generated by a turbulence generator proposed by Klein et al. [40]. There, the turbulence intensity and the integral length scale are set to $u' = 0.46$ m/s and $L_t = 2$ mm.

For both burner configurations, premixed methane/air mixture at the equivalence ratio $\Phi = 0.9$ and the initial temperature $T_0 = 300$ K is used. The system pressure is varied to from $p = 1$ bar to 5 bar. These operating conditions are selected according to the existing database of high-pressure combustion experiments for methane/air mixtures [3, 14, 16, 21, 34].

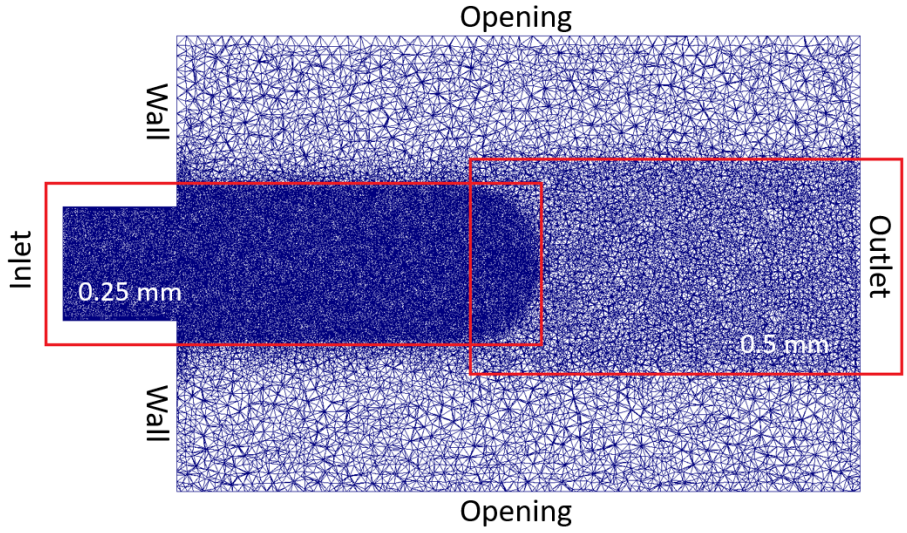


**Fig. 3** Computational grid used for LES of the Bunsen flame.

The OpenFOAM code [38] is used to solve the set of governing equations in their compressible formulation. The solution procedure employs a fully implicit scheme of second order accuracy for the time derivative (three point backward) and a second order discretization scheme for the convective and diffusive terms. The pressure-implicit split-operator (PISO) technique is applied for pressure correction [41]. The $k$-equation model has been used to model the subgrid scale (sgs) Reynolds stresses, along with unity Prandtl and Schmidt numbers for sgs scalar fluxes [42]. The available dynamic mesh solver in OpenFOAM has been applied to consider the rotation of the fans [43], which determines coordinates of the grid points according to the moving boundary by preserving spatial consistency. A more detailed description of the dynamic mesh approach can be found in [43, 44].

To evaluate chemical scalars based on $\tilde{c}$, flame profiles are pre-computed for 1D freely-propagating, unstrained premixed methane/air flames at different pressure conditions. The species mass fractions are projected onto the $c$-space, leading to a chemistry look-up table with the mass fractions of each species of functions of $c$, i.e., $Y_k = f(c)$. The open-source thermo-chemical library Cantera [45] has been used to perform the 1D flame calculations along with the GRI-3.0 reaction mechanism [46]. In this work, the reaction progress variable $c$ is determined based on the oxygen mass fraction

$$c = \frac{Y_{O_2} - Y_{O_2,ub}}{Y_{O_2,br} - Y_{O_2,ub}} \tag{6}$$

with $Y_{O_2,ub}$ and $Y_{O_2,br}$ indicating the mass fraction of $O_2$ in the unburnt and the burnt state from the 1D flame calculations. The look-up table has been built with an equidistant resolution of $\Delta c = 0.01$. Figure 4 illustrates profiles of mass fractions of some main chemical species in progress variable space at different pressures. In all cases, $Y_{O_2}$ decreases linearly with $c$, which is prescribed by the definition of $c$ with Eq.(6). In addition, there are only small differences between profiles of the main species for varied pressure conditions. This results in a similar flame temperature for different pressure conditions at around 2140 K.

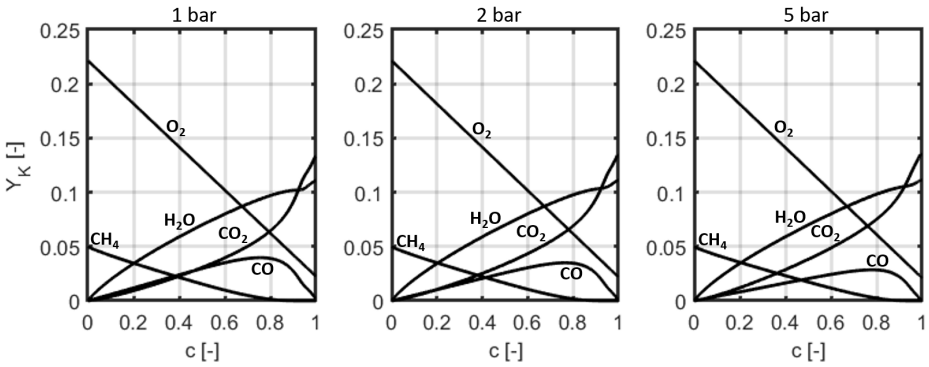


**Fig. 4** Profiles of mass fractions of some main chemical species in the progress variable domain at different pressures.

A list of laminar flame parameters as functions of pressure are provided in Tab.1, which are obtained from Cantera with calculations of 1D unstretched,

premixed propagating flames. The laminar flame thickness $\delta_L$ is given by $\delta_L = (T_{max} - T_{min})/\max|\nabla T|$ deduced from the temperature profile [37]. $Y_{\mathrm{Fu|R_{max}}}$ is used to define the flame surface in this work, which corresponds to the mass fraction of $CH_4$ at its largest negative reaction rate. As illustrated in Fig.5, the laminar flame speed $S_L$ and flame thickness $\delta_L$ compare well with the estimated data from asymptotic flame theory [37] (solid line), which predicts $S_L$ and $\delta_L$ decrease with the square root of pressure

$$a_0 \propto p^{-1}, \quad S_L \propto \sqrt{\frac{a_0}{\tau_c}} \propto p^{-1/2}, \quad \delta_L \propto \frac{a_0}{S_L} \propto p^{-1/2} \tag{7}$$

As $\rho_0$, $S_L$ and $a_0$ are directly used to calculate the mean rate $\bar{\dot{\omega}}_c$ (see Eq.(2-3)), the influence of pressure is implicitly considered by the current combustion model.

**Table 1** Laminar flame parameters derived from 1D unstrained flame calculations with Cantera for methane/air combustion at $\phi = 0.9$, $T_0 = 300$ K and $p = 1,\ 2,\ 5$ bar.

| $p$ [bar] | $S_L$ [cm/s] | $\delta_L$ [mm] | $\rho_0$ [kg/m$^3$] | $a_0$ [cm$^2$/s] | $Y_{\mathrm{Fu|R_{max}}}$ |
|---|---|---|---|---|---|
| 1 | 33.51 | 0.47 | 1.1123 | 2.828e-5 | 4.93e-3 |
| 2 | 25.42 | 0.29 | 2.2246 | 1.414e-5 | 4.12e-3 |
| 5 | 16.52 | 0.16 | 5.5615 | 4.57e-6 | 3.2e-3 |

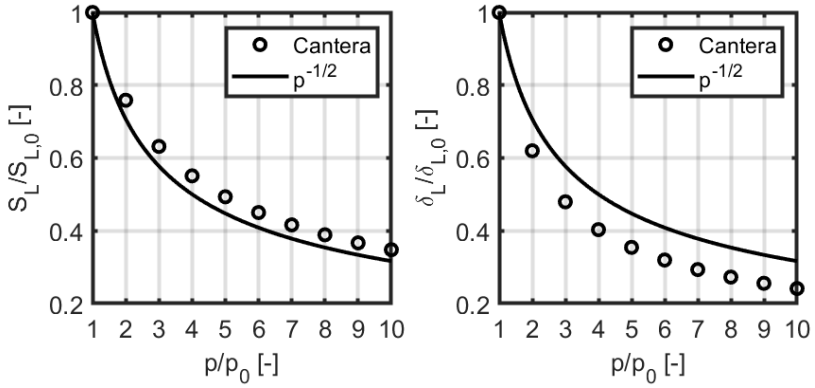


**Fig. 5** Comparison of laminar flame speed (left) and laminar flame thickness (right) from 1D flame calculations and thermal theory for different pressures ($p_0 = 1$ bar).

## 4 Simulation Results

### 4.1 Fan-stirred Combustion Bomb

#### *4.1.1 Non-Reactive Turbulent Flow Field*

In order to initialize the turbulent flow field prior to ignition, non-reactive flow simulations have first been performed for different pressure conditions. Figure 6 shows instantaneous contours of the magnitudes of velocity $|\mathbf{v}|$ (top) and the vorticity $|\nabla \times \mathbf{v}|$ (bottom) for a cross-section plane passing through the center point, as indicated in Fig.6 on the left. Both $|\mathbf{v}|$ and $|\nabla \times \mathbf{v}|$ are of the same order of magnitude for different pressures, which are largest near the rotating fans and smallest at the axes of symmetry and in the core region of the vessel. The reason is the flow field is determined by the rotation speed of the fans, which remains the same for different pressure cases. A closer look at the vorticity at the bottom of Fig.6 reveals however smaller vortices at elevated pressures, which is caused by the increased turbulent Reynolds number at elevated pressure

$$Re_T = \frac{u' L_T}{\nu} \propto p^1, \quad \text{with} \quad \nu \propto p^{-1} \tag{8}$$

as the kinematic viscosity $\nu$ decreases proportionally with pressure. The increase of $Re_T$ leads to a decrease of the Taylor and Kolmogorov length scales $\lambda$ and $\eta$ according to [47,48]

$$\lambda \propto Re_T^{-1/2} \propto p^{-1/2}, \quad \eta \propto Re_T^{-3/4} \propto p^{-3/4} \tag{9}$$

Hence, the turbulence spectrum shifts to higher wave numbers and more small-scale vortices are apparent at elevated pressures.

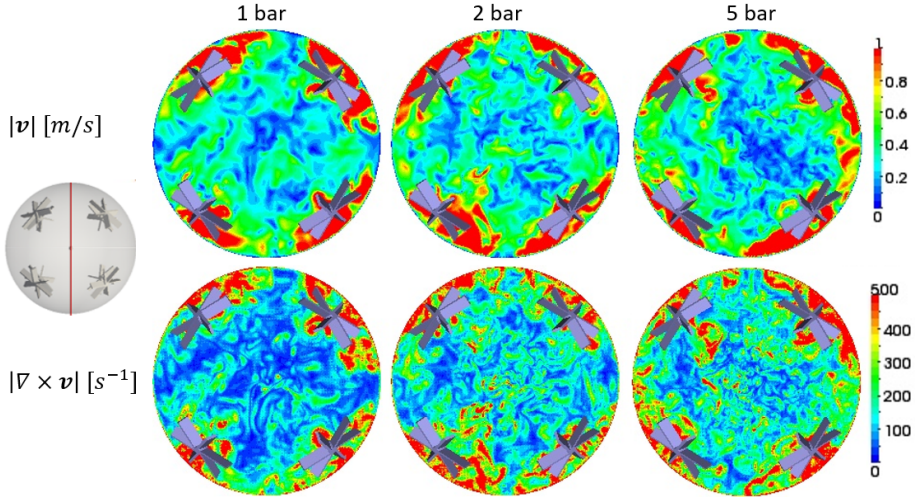


**Fig. 6** Instantaneous contours of flow velocity (top) and vorticity (bottom) calculated from LES of a fan-stirred combustion bomb at different operating pressures.

Figure 7 depicts spectra of the resolved turbulent kinetic energy $k$ at the central point of the vessel ($r = 0$). The solid line in Fig.7 identifies the $-5/3$ slope, corresponding to the inertial subrange from the Kolmogorov theory [48]. The spectra have been evaluated based on the temporal fluctuations of the resolved flow velocities $k = \frac{1}{2}(\mathbf{v}-\bar{\mathbf{v}})^2$, where $\bar{\cdot}$ indicates the operator for time averaging. The distributions of $E_k$ obtained for different pressures are similar in the spectral domain, which decreases from the low frequency range to the high frequency range. However, an increase of $E_k$ with pressure can be detected in the moderate frequency range with $f \approx 100 - 200$ Hz, denoting a larger kinetic energy of small-scale turbulent eddies at elevated pressures. This behaviour can again be explained by the increased $Re_T$ with pressure, which shifts the energy spectrum of turbulence towards the high frequency or wave number range.

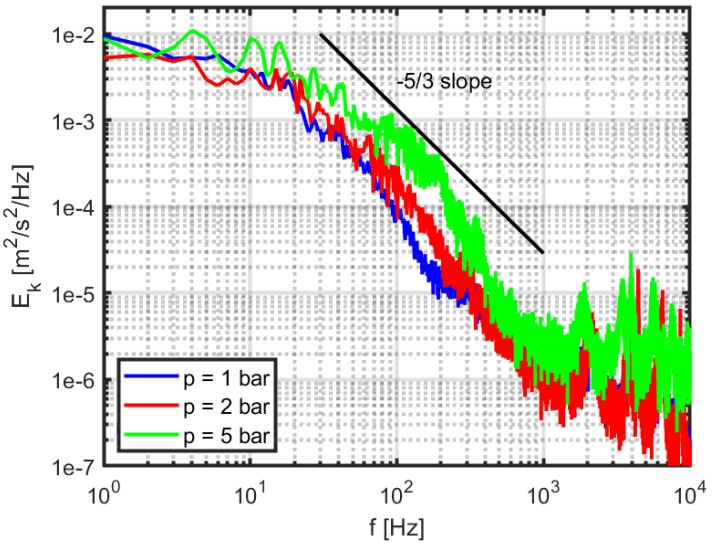


**Fig. 7** Comparison of calculated spectra of turbulent kinetic energy for 3 different pressures at the centre of the fan-stirred bomb.

It is noteworthy that dissipation of the resolved turbulent kinetic energy is perceptible at the cell length scale through a joint effect of turbulent and numerical dissipation, whereas, in reality, the turbulent kinetic energy starts to dissipate at the Kolmogorov length due to molecular diffusion. As the same computational grid is used in this work, the decay of $E_k$ in the high frequency range is similar for different pressures due to resolving the turbulent fluctuations down to the cut-off scale. The energy spectra of $E_k$ increase again at $f \approx 2000$ Hz, which is caused by the reflections of pressure waves at the vessel wall. In this case, a standing wave in radial direction emerges due to the use of the compressible formulation of the governing equations, leading to oscillations of flow variables within the whole chamber. The oscillating frequency corresponds to $f = a/L \approx 2000$ Hz, with the speed of sound at $a = \sqrt{\kappa RT} \approx 340$ m/s (for pure air at $T = 300$ K) and the wave length $L = 0.16$ m given by the diameter of the vessel.

As a summary it can be stated that elevated pressure leads to reinforced turbulent fluctuations for small-scale vortices. This however plays only a subordinate role on the integral turbulence properties, as they are by orders of magnitude smaller than the turbulent fluctuations in the low frequency range. Therefore, the calculated turbulence intensities and integral lengths for different pressures are essentially similar for the current setup. The same behaviour was also reported in [3,13], because these integral turbulence properties are determined mainly by the geometrical dimensions and the rotation speed of the fans.

### *4.1.2 Turbulent Flame Propagation*

After a statistically converged flow field is obtained from the non-reactive turbulent flow simulations, ignition of the mixture has been accomplished by using a reaction rate of $\bar{\omega}_{Ign} = 200$ kg/m$^3$/s for a central sphere zone of 2 mm diameter and a duration of 2 ms. The ignition source creates an initial flame kernel, which develops further in the turbulent flow field. Figure 8 illustrates the evolution of calculated 3D flame surface at different pressures and for a time series at $t = 4$, 8, 12 ms after ignition. There, the flame surface is identified with iso-contours of $CH_4$ mass fraction as given in Tab.1. For all time instants, the flame surface is corrugated stronger in case of elevated pressure, leading to an increased flame surface area. Considering the effect of pressure on the flame-turbulence interaction, the turbulent Damköhler number is rather insensitive to pressure, as the integral turbulence parameters and the chemical time scale remain mostly unchanged with

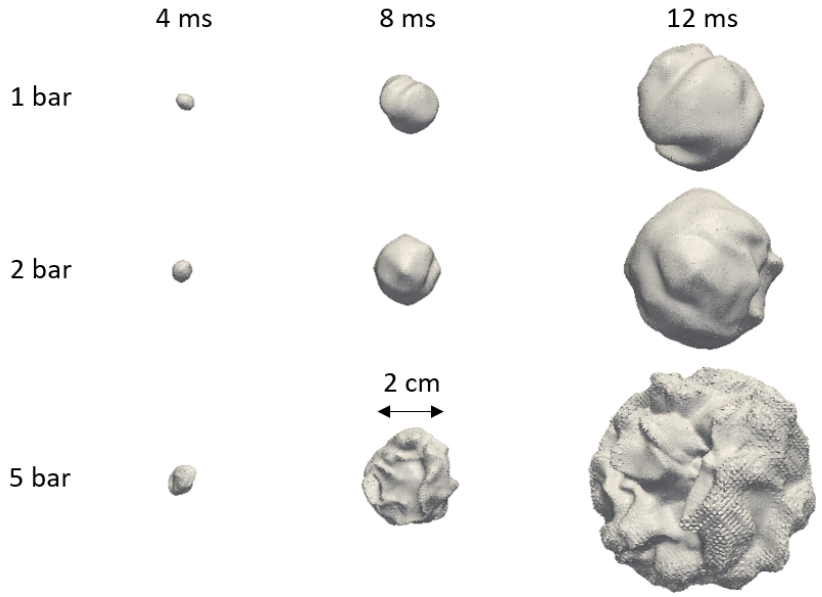


**Fig. 8** Temporal evolution of calculated 3D flame surface in a fan-stirred combustion bomb.

varied pressure

$$Da_T = \frac{\tau_T}{\tau_C} \propto \frac{L_T/u'}{a_0/S_L^2} \propto p^0 \tag{10}$$

The turbulent Karlovitz number however increases with pressure, because the Kolmogorov length $\eta$ decreases faster than the laminar flame thickness $\delta_L$ with pressure, as shown in Eq.(7) and Eq.(9)

$$Ka_T = (\delta_L/\eta)^2 \propto p^{1/2} \tag{11}$$

Therefore, an enhanced flame-turbulence interaction towards stronger wrinkled and torn flame surface is expected at elevated pressure.

In Fig.9, instantaneous contours of the turbulent mean rate $\bar{\dot{\omega}}_c$ for the time instant $t = 8$ ms are used to identify the resolved reaction zones. The enlargement of flame surface with pressure can be detected again. The magnitude of the mean reaction rate $\bar{\dot{\omega}}_c$ (see Eq.(2)) increases excessively with pressure (see the color legends in Fig.9), indicating a contribution of increased turbulent fluctuations in addition to the proportional increase of $\rho_0$ with pressure. The resolved flame thickness with $\bar{\dot{\omega}}_c > 0$ remains almost constant at different pressures, although the laminar flame thickness decreases with pressure (see Tab.1). In fact, as the laminar flame thickness of the order of $\mathcal{O}(0.1$ mm) cannot be resolved on the LES grid, the flame front is filtered out on the cut-off scale in the simulations. In addition, the formulation of mean rate used by the current TFC model with $\bar{\dot{\omega}}_c \propto \tilde{c}(1-\tilde{c})$ reproduces a spatially averaged flame front, which is essentially thick compared with the intrinsic flame front [36]. Nonetheless, the proposed numerical approach is able to reproduce qualitatively an enhanced flame-wrinkling at increased pressure, which agrees with previous high pressure combustion experiments [3, 8, 11–14, 21].

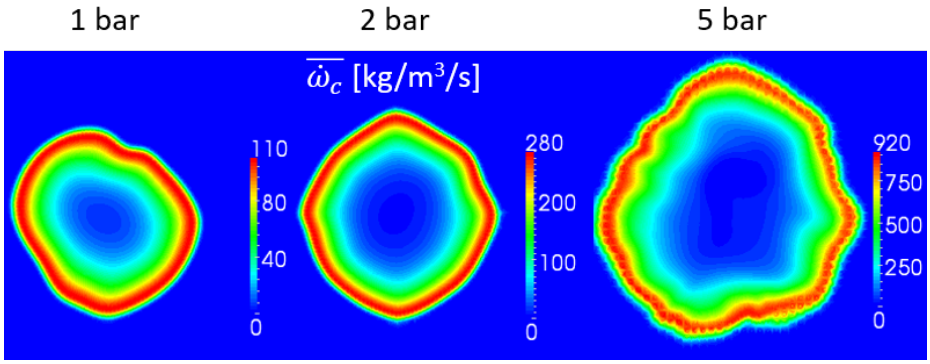


**Fig. 9** Contours of mean reaction rates at different pressures and for the same time instant.

The behaviour of increased burning rate with pressure is further illustrated by the temporal evolution of the total burning rate $R$ and the total flame surface area $A_F$ shown in Fig.10, where $R$ is calculated by the volume integration of $\bar{\dot{\omega}}_c$ over the entire computational domain (see Eq.(12)). The numerical simulations predict an increase of $R$ and $A_F$ with pressure, where the growth rate of $R$ or $A_F$ from 2 to 5 bar is considerably higher compared to that from 1 to 2 bar. This reveals

a stronger influence of pressure on the overall burning rate in the high pressure range.

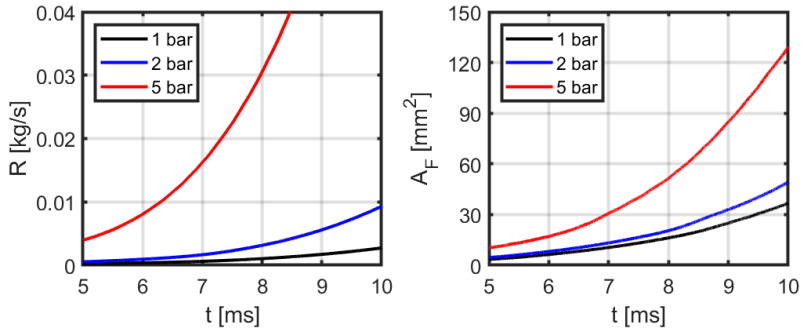


**Fig. 10** Temporal developments of the overall burning rate (left) and the flame surface area (right) under different pressure conditions.

In general, the artificial flame front resolved by LES cannot represent the real flame. Therefore, the current work focuses on the overall consumption rate $R$ as a more suitable parameter for the actual flame surface area. In this way, $R$ is further normalized with $A_F$ to obtain the turbulent consumption speed $S_C$

$$S_C = \frac{R}{\rho_0 A_F}, \quad R = \int_V \bar{\dot{\omega}}_c \mathrm{d}V \tag{12}$$

$S_C$ represents a measure of the overall burning rate and considers the effect of flame-turbulence interactions at elevated pressures. Note that $S_C$ differs from the sgs turbulent flame speed $S_{T,sgs}$ (see Eq.(3)) used for modeling the mean rate, which is locally evaluated for each individual cell volume. In Fig.11, $S_C$ is calculated for two different cases with ignition of the flame under quiescent (left) and turbulent flow (right) conditions. The same numerical setups and equations have been applied for both scenarios. The flame speed $S_C$ decreases with pressure in the laminar flow case, which is in accordance with results obtained from 1D

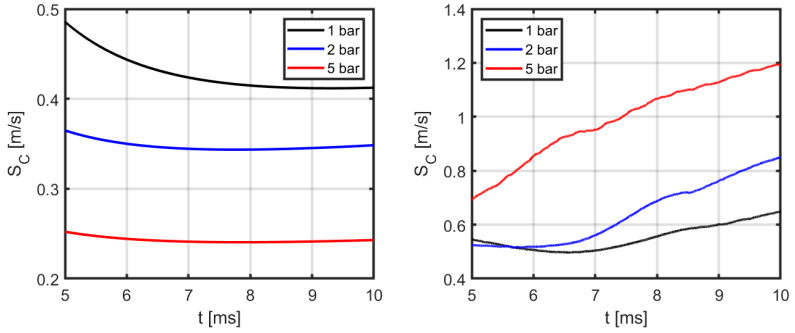


**Fig. 11** Comparison of calculated mean consumption speed at different pressures: on the left under laminar flow condition and on the right under turbulent flow condition.

laminar flame calculations (see the left subplot of Fig.5). On the contrary, $S_C$ increases with pressure under turbulent flow conditions. Therefore, the increase of overall burning rate at elevated pressure is attributable to the enhanced turbulent fluctuations as well as their interactions with the flame.

Figure 12a depicts developments of the equivalent flame radii $r_F = \sqrt{A_F/\pi}/2$ and Fig.12b shows the total burning rate $R$ with respect to $r_F$ at different pressure conditions. Based on these parameters, the turbulent consumption speed $S_C$ (solid line, see Eq.(12)) and displacement speed $S_D$ (dashed line)

$$S_D = \frac{\rho_b}{\rho_0}\frac{\mathrm{d}r_F}{\mathrm{d}t}, \quad \rho_b - \text{density of burnt gas} \tag{13}$$

are calculated and plotted in Fig.12c as functions of $r_F$ for the evaluation range 15 mm $< r_F <$ 30 mm or $19 < r_F/r_{Vessel} < 38$, to avoid ignition and wall effects at the initial and final stages of flame propagation [21]. $S_C$ and $S_D$ are larger at elevated pressure, which corresponds to the faster increase of $r_F$ and $R$ at higher pressures, as shown in Fig.12a and Fig.12b. $S_C$ is however larger compared with $S_D$, which is due to defining the flame surface on the flame's trailing edge with $Y_{CH_4} = Y_{\mathrm{Fu|R_{max}}}$ (see Tab.1), leading to a relatively small $A_F$ or large $S_C$ due to $S_C \propto 1/A_F$. In Fig.12c, $S_C$ and $S_D$ increase slightly with $r_F$ for all pressure conditions, denoting an acceleration of flame propagation with increasing $r_F$. This is attributable the fact that as the flame expands during propagation, its smallest wave number decreases resulting in a continuous increase in the integral flame dissipation spectrum [21,22]. In addition, the increase of turbulence intensity with flame radii may contribute to the acceleration of flame propagation.

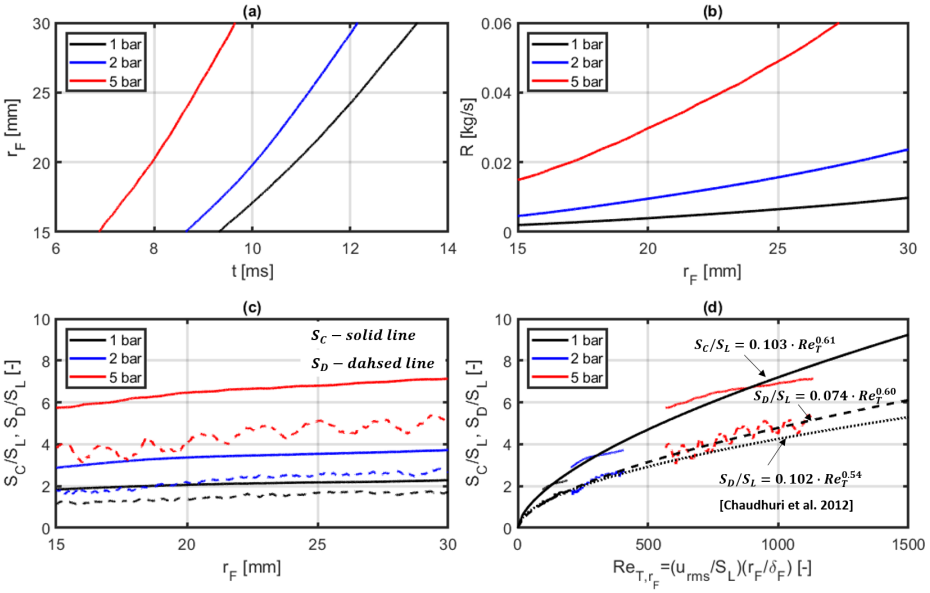


**Fig. 12** Top: temporal evolutions of flame radii $r_F$ (left) and progress of the overall consumption rate $R$ over the flame radii (right). Bottom: Normalized consumption and displacement speeds $S_C$ (solid line) and $S_D$ (dashed line) with respect to $r_F$ (left) and the turbulent Reynolds number based on $r_F$ (right) for the evaluation range of 15 mm $< r_F <$ 30 mm.

Figure 12d plots $S_C$ and $S_D$ normalized by $S_L$ with respect to the turbulent Reynolds number based on the flame radii $Re_{T,r_F} = (u_{rms}/S_L) \cdot (r_F/\delta_F)$ for the same evaluation range used in Fig.12c, showing a self-similar propagation behaviour as found in [21] and further experimentally confirmed in [16,22] for outwardly expanding flames. In this case, all data pairs $S_C/S_L$ or $S_D/S_L$ vs. $Re_{T,r_F}$ from different conditions and instants of flame propagation collapse reasonably well on a power law curve with the form $S_{C,D}/S_L = a \cdot Re^b_{T,r_F}$. The power exponent $b$ obtained from nonlinear least-square fitting over the entire data range, indicated in Fig.12d, is approximately equal to $b = 0.6$ for both $S_C$ and $S_D$, which is slightly larger compared with the measured exponent with $b = 0.54$ [16,21,22]. One reason may be that evaluating $S_C$ and $S_D$ with the total consumption rate and a 3D flame surface in this work, whereas only 2D cuts of the flame surface were used in experiments. In addition, the under-resolved flame front and its interaction with the turbulent fluctuations by LES combustion modeling may contribute to this difference too. Nonetheless, the correlations of $S_D/S_L$ vs. $Re_{T,r_F}$ derived from the simulations (dashed line) and experiments (dotted line) show a reasonably good agreement for the pressures conditions with $p = 1$ bar and $p = 2$ bar, and the differences between these curves at 5 bar are fairly within the uncertainty range of the measurement data [21].

As the definition of the flame surface by an iso-surface has a strong impact on $S_C$, $S_C$ cannot be compared directly with measured flame speed. Therefore, the amplification rate $\gamma_p$ of the flame wrinkling factor $\Xi$ in terms of the ratios of $S_C$ or $S_D$ at different pressures are used for demonstrating the ability of the proposed model for reproducing the enhanced burning effect at elevated pressure, with the reference pressure set to $p_{ref} = 1$ bar

$$\gamma_p = \frac{\Xi_p}{\Xi_{p_{ref}}} = \frac{(S_T/S_L)_p}{(S_T/S_L)_{p_{ref}}} \tag{14}$$

$\Xi$ represents generally a measure of increased flame surface area or burning rate due to flame-turbulence interaction. Different correlations for $\Xi$ have been proposed based on high-pressure experimental studies of hydrocarbon flames, which consider the effect of increased operating pressure

– Kobayashi et al. [14]:

$$\Xi = \frac{S_T}{S_L} = 5.0 \left( \frac{u'}{S_L} \cdot \frac{p}{p_{ref}} \right)^{0.38} \tag{15}$$

– Jiang et al. [16]:

$$\Xi = \frac{S_T}{S_L} = 2.88 \left( \frac{u'}{S_L} \cdot \frac{p}{p_{ref}} \right)^{0.41} \tag{16}$$

– Dinkelacker et al. [34]:

$$\Xi = \frac{A_T}{\bar{A}} = 1 + \frac{0.46}{Le} Re_T^{0.25} \left( \frac{u'}{S_L} \right)^{0.3} \left( \frac{p}{p_{ref}} \right)^{0.2} \tag{17}$$

These correlations are derived from fitting measured data of turbulent flame speed at varied pressures from different experimental setups with Bunsen-type flames [14,

34] and outwardly expanding flames in fan-stirred bombs [16]. The equations (15-17) reveal a growth of the wrinkling factor with pressure $\Xi \propto \left(\frac{p}{p_{ref}}\right)^{\beta}$ in form of a power-law function, with an almost constant exponent of $\beta \approx 0.4$ (note that $Re_T$ in Eq.(17) is proportional to pressure, as shown in Eq.(8)). Table 2 lists $\gamma_p$ derived from LES and Eq.(15-17), where the calculated $\gamma_p$ corresponds to the ratio of $S_{C,D}$ at elevated pressures to $S_{C,D}$ at $p_{ref} = 1$ bar (see Fig.12c). There, only the values in the range of $19 < r_F/r_{Vessel} < 38$ are used in order to avoid the influences of ignition and wall, as shown in Fig.12c. For the evaluation of $\gamma$ from Eq.(15-17), the integral turbulence properties $u'$ and $L_t$ are assumed to be constant with varied pressure.

| p [bar] | LES-$S_C$ | LES-$S_D$ | Eq.(15) [14] | Eq.(16) [16] | Eq.(17) [34] |
|---|---|---|---|---|---|
| 2 | 1.62 | 1.51 | 1.45 | 1.49 | 1.48 |
| 5 | 3.12 | 2.92 | 2.36 | 2.53 | 2.51 |

**Table 2** Comparison of calculated and measured amplification of flame wrinkling factor at elevated pressures.

The measured $\gamma$ by using the correlations Eq.(15-17) compare well with each other, as the power exponent for $\Xi$ is nearly constant with respect to $p/p_{ref}$. The computed $\gamma$ from LES is however larger than the measured data and the difference is more distinctive for $p = 5$ bar. One reason may be attributed to assuming a constant turbulence intensity $u'$ by using Eq.(15-17), whereas enhanced small-scale turbulent fluctuations are confirmed at elevated pressure in the simulations (see Sec.4.1.1). In addition, the current LES evaluates $S_C$ and $S_D$ in terms of the overall consumption rate (see Eq.(12)) and a 3D flame surface (see Eq.(13)), whereas the cone angle for the Bunsen-flame and 2D cuts of the 3D flame surface for the outwardly expanding flame were used for determining $S_T$ in the experiments. Despite these differences, the experimentally observed influence of elevated pressure on the turbulent flame propagation, which is given by the enhanced flame wrinkling and overall burning rate, can be reproduced by using the current TFC-LES approach.

### 4.2 Bunsen-type Flame

Unlike the purely transient, outwardly expanding flame, the Bunsen burner yields a quasi-steady flame in the time-average, which represents another important class of flame in practice. This configuration allows evaluating the turbulent burning velocity based on the mean cone angle, which is used in the following as a further support of the results obtained for the expanding flame and validation of the proposed LES approach with respect to the effect of elevated pressure. In this context, the proposed numerical model has been applied to the Bunsen-burner configuration experimentally studied by Kobayashi et al. [14]. Again, premixed methane/air mixture at $\Phi = 0.9$, $T_0 = 300$ K has been used and the pressures are $p = 1$ bar and $p = 5$ bar, employing otherwise the same numerical setups, boundary conditions and computational grid (see Sec.3). Figure 13 depicts instantaneous contours of

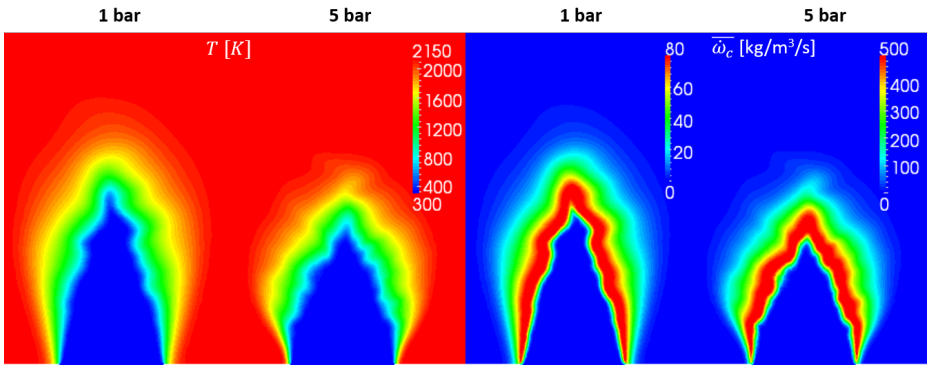


**Fig. 13** Contours of calculated temperature (left) and reaction rate (right) from LES of a Bunsen-type flame at different pressures.

the temperature $T$ and the resolved mean rate $\bar{\dot{\omega}}_c$. The flame temperature remains almost unaffected by the pressure, whereas the burning rate is increased disproportionately with pressure. In addition, the flame is shorter at elevated pressure, confirming a higher overall burning rate. Figure 14 on the left depicts instantaneous flame surfaces identified by $\tilde{c} = 0.5$, where a stronger wrinkling of the flame surface can be detected for the high pressure case. This results in an enhanced flame-turbulence interaction and a shorter flame, as shown on the right of Fig.14 by the time mean contours of $\tilde{c}$, with the solid lines indicating the time mean $\tilde{c} = 0.5$ contours.

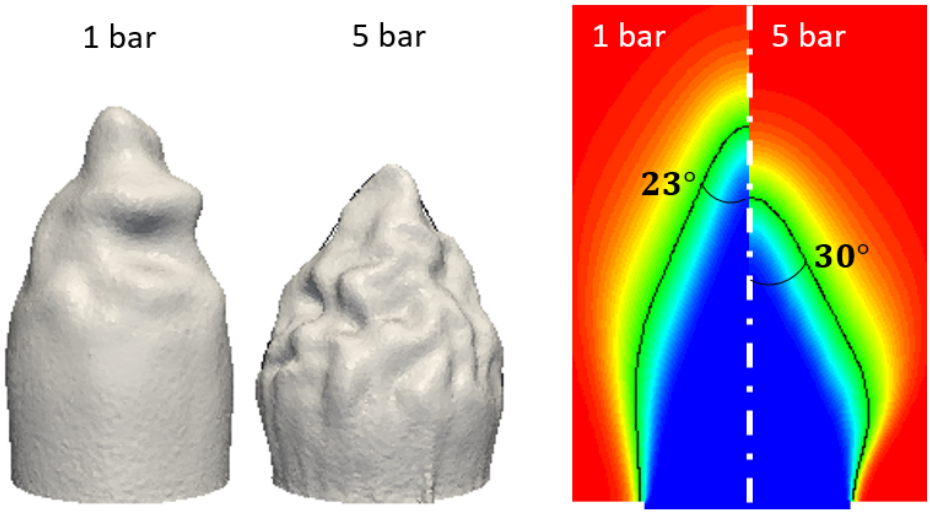


**Fig. 14** Instantaneous flame surfaces calculated from LES of a Bunsen-type flame (left) and comparison of time mean contours of $\bar{c}$ at different pressures (right).

The turbulent flame speed derived from the cone angle $\alpha$ of the jet flame, as indicated in Fig.14 on the right, yields

$$\left(\frac{S_T}{S_L}\right)_{1\ \mathrm{bar}} = 2.75 \quad \text{and} \quad \left(\frac{S_T}{S_L}\right)_{5\ \mathrm{bar}} = 7.14 \quad \text{with } S_T = u_0\ \sin\alpha \tag{18}$$

By using the calculated rms values of turbulent fluctuations $u' = u_{rms}$ at the center of the burner outlet according to [14] ($u'_{1\ \mathrm{bar}} = 0.2$ m/s and $u'_{5\ \mathrm{bar}} = 0.24$ m/s), the results given by Eq.(18) compare quantitatively well with the measured dependencies of $S_T/S_L$ vs. $u'/S_L$ from [14]. The amplification of the wrinkling rate due to increased pressure is calculated to

$$\gamma = \frac{(S_T/S_L)_{5\ \mathrm{bar}}}{(S_T/S_L)_{1\ \mathrm{bar}}} = 2.60 \tag{19}$$

which shows a good agreement with results obtained from the measured correlations in Eq.(15-17) (see Tab.2 for $p = 5$ bar). In comparison with $S_T$ derived from the flame's cone angle in Eq.(18), $S_C$ based on the overall consumption rate can be evaluated from the simulations by using Eq.(12)

$$\left(\frac{S_C}{S_L}\right)_{1\ \mathrm{bar}} = 1.73 \quad \text{and} \quad \left(\frac{S_C}{S_L}\right)_{5\ \mathrm{bar}} = 4.28 \tag{20}$$

with the flame surfaces $A_F$ specified by the same iso-surfaces of $Y_{\mathrm{CH_4}} = Y_{\mathrm{Fu|R_{max}}}$ (see Tab.1), as used in the last section for the bomb setup. These lead to

$$\gamma = \frac{(S_C/S_L)_{5\ \mathrm{bar}}}{(S_C/S_L)_{1\ \mathrm{bar}}} = 2.47 \tag{21}$$

considering the effect of pressure on the amplification of the overall burning rate. Hence, the use of different flame configurations, i.e., the enclosed bomb setup or the Bunsen burner, and different evaluation methods for $S_T$, i.e., using consumption rate, displacement speed or cone angle, have an influence on the calculations of $\gamma$.

Despite these differences, the proposed numerical simulations are able to reproduce characteristic behaviours of increased consumption rate due to the enhanced flame wrinkling at elevated pressure. The calculated growth rate of flame wrinkling by increased pressure shows a reasonably good agreement with the measured data derived from different flame configurations, without using additional adjustment parameters. The Karlovitz number has been confirmed to be larger than unity for all simulation conditions used in this work. Therefore, the mechanism responsible for flame wrinkling is outside the regime affected by the Darrieus–Landau instability according to the revised flame regime diagram proposed in [25,26]. In addition, the laminar flame speed $S_L$ is assumed to be unaffected by flow stretch. Hence, the statement with a decreased Markstein number or locally increased burning velocity due to flow stretch for explaining the reinforced burning rate at elevated pressure is not valid in this case, too. Therefore, the main mechanism leading to a higher burning rate and flame wrinkling at elevated pressure is due to the enhanced turbulent fluctuations by small-scale vortices, which results in a more intense flame-turbulence interaction.

## 5 Conclusion

Numerical simulations of a laboratory-scale, fan-stirred combustion bomb and a Bunsen-type flame have been performed to study the effect of elevated pressure on turbulent flame propagation. The objective is to reveal the main mechanism of increased flame wrinkling due to elevated pressure, and to assess the applicability of the turbulent flame-speed closure (TFC-class) combustion model combined with the large eddy simulation (LES) technique in reproducing this effect. The beneficial effect of elevated pressure on the overall burning rate is explained by the generation of small-scale flame structures due to reinforced small-scale turbulent fluctuations, which largely compensates the reduction of laminar flame speed at high pressure. The current TFC combustion model in the framework of LES reproduces an enhanced flame wrinkling and overall burning rate at elevated pressure. The calculated growth rates of the flame wrinkling factor due to increased pressure compare well with measured data from different flame configurations.

Despite the fact that small-scale flame curvatures (smaller than the cut-off length) cannot be resolved by the TFC-LES, the obtained results yield a reasonably good agreement with diverse measured correlations regarding the effect of pressure on the flame-turbulence interaction. The simulations provide additional useful information with more detailed insight into the underlying chemo-physical processes, which is not accessible from experiment. Therefore, it can be stated that the numerical approach with TFC-LES used in this work is suited for modeling high pressure combustion applications, which may be integrated into tools of computer aided designs for future combustion systems.

**Acknowledgements** The authors gratefully acknowledge the financial support by the Helmholtz Association of German Research Centers (HGF), within the research field Energy, Material and Resources, Topic 4 Gasification (34.14.02). This work utilized computing resources from the Steinbuch Centre for Computing (SCC) at the Karlsruhe Institute of Technology (KIT).

## Compliance with Ethical Standards

The authors declare that they have no conflict of interest.

## References

1. Bradley, D., Lawes, M., Mansour, M.S.: Explosion bomb measurements of ethanol-air laminar gaseous flame characteristics at pressures up to 1.4 MPa. Combust. Flame **156**(7), 1462-1470 (2009).
2. Bradley, D., Lawes, M., Liu, K., Verhelst S., Woolley, R.: Laminar burning velocities of lean hydrogen–air mixtures at pressures up to 1.0 MPa. Combust. Flame **149**(1-2), 162-172 (2007).
3. Kobayashi, H.: Experimental study of high-pressure turbulent premixed flames. Exp. Therm Fluid Sci. **26**(2-4), 375-387 (2002).
4. Hu, E., Huang, Z., He, J., Zheng, J., Miao, H.: Measurements of laminar burning velocities and onset of cellular instabilities of methane-hydrogen-air flames at elevated pressures and temperatures. Int. J. Hydrog. Energy **34**(3), 5574-5584 (2009).
5. Wang, J., Yu, S., Zhang, M:, Jin, W., Huang, Z., Chen, S., Kobayashi, H.: Burning velocity and statistical flame front structure of turbulentpremixed flames at high pressure up to 1.0 MPa. Exp Therm Fluid Sci **68**, 196-204 (2015).

6. Bradley, D., Hicks, R.A., Lawes, M., Sheppard, C.G.W., Woolley, R.: The Measurement of Laminar Burning Velocities and Markstein Numbers for Iso-octane-Air and Iso-octane–n-Heptane-Air Mixtures at Elevated Temperatures and Pressures in an Explosion Bomb, Combust. Flame **115**(1-2), 126-144 (1998).
7. Hassan, M.I., Aung, K.T., Kwon, O.C., Faeth, G.M.: Properties of laminar premixed hydrocarbon/air flames at various Pressures. J Propul Power **14**(4), 479 (1998).
8. Kitagawa, T., Nakahara, T., Maruyama, K., Kado, K., Hayakawa, A., Kobayashi, S.: Turbulent burning velocity of hydrogen-air premixed propagating flames at elevated pressures. Internat. J. Hyd. Energy **33**(20), 5842-5849 (2008).
9. Vukadinovic, V., Habisreuther, P., Zarzalis, N., Suntz, R.: Influence of Pressure on Markstein Number Effects in Turbulent Flame Front Propagation. Proceedings of ASME Turbo Expo, GT2013-94307 (2013).
10. Zirwes, T., Zhang, F., Denev, J.A., Habisreuther, P., Bockhorn, H.: Effect of Elevated Pressure on Markstein Number of Lean-Premixed Methane-Air Flames. Proceedings of the 28th Deutscher Flammentag, 549 (2017)
11. Soika, A., Dinkelacker, F., Leipertz, A.: Pressure influence on the flame front curvature of turbulent premixed flames: comparison between experiment and theory. Combust. Flame **132**(3), 451-462 (2003).
12. Fragner, R., Halter, F., Mazellier, N., Chauveau, C., Gökalp, I.: Investigation of pressure effects on the small scale wrinkling of turbulent premixed Bunsen flames. Proc. Combust. Inst **35**(2), 1527-1535 (2015).
13. Lachaux, T., Halter, F., Chauveau, C., Gökalp, I., Shepherd, I.G.: Flame front analysis of high-pressure turbulent lean premixed methane–air flames. Proc. Combust. Inst **30**(1), 819-826 (2005).
14. Kobayashi, H., Seyama, K., Hagiwara, H., Ogami, Y.: Burning velocity correlation of methane/air turbulent premixed flames at high pressure and high temperature. Proc. Combust. Inst **30**(1), 827-834 (2005).
15. Liu, C., Shy, S., Peng, M., Chiu, C., Dong, Y.: High-pressure burning velocities measurements for centrally-ignitedpremixed methane/air flames interacting with intense near-isotropic turbulenceat constant Reynolds numbers. Combust. Flame **159**(8), 2608-2619 (2012).
16. Jiang, L.J., S.S. Shy, Li, W.Y., Huang H.M., M.T. Nguyen: High-temperature, high-pressure burning velocities of expanding turbulent premixed flames and their comparison with Bunsen-type flames. Combust. Flame **172**, 173-182 (2016).
17. Chaudhuri, S., Saha, A., Law, C.K.: On flame–turbulence interaction in constant-pressure expanding flames. Proc. Combust. Inst **35**(2), 1331–1339 (2015).
18. Bradley, D., Lawes, M., Mansour, M.: Correlation of turbulent burning velocities of ethanol–air, measured in a fan-stirred bomb up to 1.2 MPa. Combust. Flame **158**(1), 123-138 (2011).
19. Nguyen, M., Yu, D., Shy, S.: General correlations of high pressure turbulent burning velocities with the consideration of lewis number effect. Proc. Combust. Inst **37**(2), 2391–2398 (2019).
20. Ichikawa, A., Naito, Y., Hayakawa, A., Kudo, T., Kobayashi, H.: Burning velocity and flame structure of ch4/nh3/air turbulent premixed flames at high pressure. Int. J. Hydrog. Energy **44**(13), 6991–6999 (2019).
21. Chaudhuri, S., Wu, F., Zhu, D., Law, C.K.: Flame speed and self-similar propagation of expanding turbulent premixed flames. Phys. Rev. Lett. **108**(4), 044503 (2012).
22. Wu, F., Saha, A., Chaudhuri, S., Law, C.K.: Propagation speeds of expanding turbulent flames of c4 to c8 n-alkanes at elevated pressures: Experimental determination, fuel similarity, and stretch-affected local extinction. Proc. Combust. Inst **35**(2) 1501–1508 (2015).
23. Lipatnikov, A.N., Chomiak, J.:Effects of premixed flames on turbulence and turbulent scalar transport. Prog. Energy Combust. **36**(1), 1–102 (2010).
24. Creta, F., Fogla, N., Matalon, M.: Turbulent propagation of premixed flames in the presence of Darrieus–Landau instability. Combust. Theory Model **15**(2), 267–298 (2011).
25. Chaudhuri, S., Akkerman, V., Law, C.K.: Spectral formulation of turbulent flame speed with consideration of hydrodynamic instability. Phys. Rev. E **84**(2), 026322 (2011).
26. Yang, S., Saha, A., Liu, Z., Law, C.K.: Role of darrieus–landau instability in propagation of expanding turbulent flames. J FLUID MECH **853**, 784–802 (2018).
27. Zhang, W., Wang, J., Guo, S., Yu, Q., Jin, W., Zhang, M., Huang, Z.: Effects of integral scale on darrieus–landau instability in turbulent premixed flames. Flow Turbul. Combust **103**(1), 225–246 (2019).

28. Chaudhuri, S., Saha, A., Law, C.K.: On flame–turbulence interaction in constant-pressure expanding flames. Proc. Combust. Inst **35**(2), 1331–1339 (2015).
29. Zimont, V. L., Lipatnikov, A.N.: A numerical model of premixed turbulent combustion of gases. Chem. Phys. Rep. **14**(7), 993-1025 (1995).
30. Schmid, H., Habisreuther, P., Leuckel, W.: A model for calculating heat release in premixed turbulent flames. Combust. Flame **113**, 79-91 (1998).
31. Flohr, P., Pitsch, H.: A turbulent flame speed closure model for LES of industrial burner flows. Proceedings of the Summer Program, Stanford Summer Program, 169-179 (2000).
32. Dinkelacker, F., Hölzler, S., Leipertz, A.: Investigations with a Turbulent Flame-Speed-Closure Model for Premixed Turbulent Flame Calculations. Combust. Sci. Technol. **158**, 321-340 (2000).
33. Zhang, F., Habisreuther, P., Hettel, M., Bockhorn, H.: Modeling of a Premixed Swirl-stabilized Flame Using a Turbulent Flame Speed Closure Model in LES. Flow Turbul. Combust **82**, 537-551, 2009.
34. Dinkelacker, F., Manickam, B., Muppala, S.P.R.: Modelling and simulation of lean premixed turbulent methane/hydrogen/air flames with an effective Lewis number approach. Combust. Flame **158**, 1742–1749 (2011).
35. Zhang, F., Habisreuther, P., Bockhorn, H., Nawroth, H., Paschereit, C.O.: On prediction of combustion generated noise with the turbulent heat release rate. ACTA ACUST UNITED AC **99**(6), 940-951 (2013).
36. Zhang, F., Zirwes, T., Habisreuther, P., Bockhorn, H., Trimis, D., Nawroth, H., Paschereit C.O.: Impact of Combustion Modeling on the Spectral Response of Heat Release in LES. Combust. Sci. Technol. **191**(9), 1520-1540 (2019).
37. Poinsot, T., Veynante, D.: Theoretical and Numerical Combustion, R.T. Edwards Inc., Philadelphia, U.S.A. (2005).
38. OpenFOAM. The Open Source CFD Toolbox. User Guide (2014). `https://www.openfoam.com/releases/openfoam-v1612+/`
39. Weiß ,M., Zarzalis, N., Suntz, R.: Experimental study of Markstein number effects on laminar flamelet velocity in turbulent premixed flames. Combust. Flame **154**(4), 671-691 (2008).
40. Klein, M., Sadiki, A., Janicka, J.: A digital filter based generation of inflow data for spatially developing direct numerical or large eddy simulations. J. Comput. Phys. **286**, 652-665 (2003).
41. Ferziger, J.H., Perić. M.: Computational Methods for Fluid Dynamics, Springer, Heidelberg (2002).
42. Fröhlich, J.: Large Eddy Simulation turbulenter Strömungen, Teubner Verlag, Germany (2006)
43. Jasak, H., Rusche, H.: Dynamic Mesh Handling in OpenFOAM `http://web.student.chalmers.se/groups/ofw5/Advanced_Training/DynamicMesh.pdf`
44. Zhang, F, Zirwes, T., Zarzalis, N., Bockhorn, H., Trimis, T.: Numerical Computation of Turbulent Flow Fields in a Fan-stirred Combustion Bomb, Combust. Sci. Technol., in press (2019).
45. Goodwin, D., Moffat, H., Speth, R.: Cantera: An object-oriented software toolkit for chemical kinetics, thermodynamics, and transport processes. version 2.3.0b (2017). Software available at `https://www.cantera.org`
46. Smith, G., Golden, D., Frenklach, M., Moriarty, N., Eiteneer, B., Goldenberg, M., Bowman, C., Hanson, R., Song, S., Jr., W.G., Lissianski, V., Qin, Z.: Gri 3.0 reaction mechanism. `http://www.me.berkeley.edu/grimech`
47. Tennekes, H., Lumley, J.L.: A first Course in Turbulence, M.I.T. Press, Cambridge, Mass., USA (1972).
48. Pope, S.B.: Turbulent Flows. Cambridge University Press, Cambridge, U.K. (2000).
49. Zhang, F., Baust, T., Zirwes, T., Denev, J., Habisreuther, P., Zarzalis, N., Bockhorn, H.: Impact of infinite thin flame approach on the evaluation of flame speed using spherically expanding flames. Energy Technol **5**, 1055-1063 (2017).